Research Square

Preprints are preliminary reports that have not undergone peer review.
They should not be considered conclusive, used to inform clinical practice,
or referenced by the media as validated information.

Droplet Wetting Synergy on Hydrophobic/Hydrophilic Dual-Phase Substrates

C. B. Lin
Tamkang University
Hung-Chou Lee
Tamkang University
Chin-Shun Leung
Tamkang University
Po-Ching Lee
pclee@mail.tku.edu.tw
Tamkang University

Research Article

Keywords: photolithography, chemical vapor deposition, hydrophobicity, hydrophilicity, contact angle, surface engineering

Posted Date: November 4th, 2026

DOI: https://doi.org/10.21203/rs.3.rs-11407174/v1

License: This work is licensed under a Creative Commons Attribution 4.0 International License.
Read Full License

Additional Declarations: No competing interests reported.

Droplet Wetting Synergy on Hydrophobic/Hydrophilic Dual-Phase Substrates

C. B. Lin[1], Hung-Chou Lee[1], Chin-Shun Leung[1], and Po-Ching Lee[2*]

[1]Department of Mechanical and Electromechanical Engineering,

[2*]Department of Water Resources and Environmental Engineering

TamKang University, Tamsui District, New Taipei City, Taiwan

[*]Corresponding Author Email: pclee@mail.tku.edu.tw

Abstract

This study fabricated alternating hydrophobic–hydrophilic micropatterned surfaces using photolithography, chemical vapor deposition, and reactive ion etching. Hydrophilic regions were flat SiO_2, while hydrophobic square patterns (10 and 40 μm) were prepared via (i) perfluorinated low-surface-energy self-assembled monolayers (SiO_2-FT-SAM), (ii) RIE-induced roughening (SiO_2/SiO_2*), and (iii) combined roughness and SAM modification (SiO_2/SiO_2*-FT-SAM). Wettability was evaluated at hydrophobic area fractions of 25%, 50%, and 75%. At 40 μm feature size and 75% coverage, the hybrid surface achieved a static contact angle of 138°, indicating a stable Cassie state with a trapped air layer. The observed reversibility of the air film further supports the synergistic roles of micro-roughness and low surface energy. Overall, this approach enables effective wettability control and supports the development of self-cleaning, low-adhesion surfaces.

Keywords: photolithography; chemical vapor deposition; hydrophobicity; hydrophilicity; contact angle; surface engineering

1. Introduction

Hydrophobic surfaces are widely used in both research and industry because of

their water-repellency and resistance to wetting, with applications including waterproofing, antifouling, corrosion protection, oil–water separation, and anti-icing. Such technologies have been incorporated into construction materials, electronic devices, automotive coatings, and textiles to reduce moisture-induced degradation of material performance and structural integrity. Achieving high hydrophobicity, or superhydrophobicity (static contact angle >150°), generally relies on two complementary strategies. The first is microstructure engineering, which increases apparent hydrophobicity by introducing micro- to nanoscale surface roughness via laser etching (Genzer and Efimenko 2000), nanoimprinting (Pozzato et al. 2006), microelectromechanical systems (MEMS) fabrication (Cottin-Bizonne et al. 2003), anodization (Tadanaga et al. 2000), nanosphere lithography (Descamps et al. 1996; Haynes and Van Duyne 2001), or electrostatic spraying (Wang et al. 2018). The second is surface-energy reduction, typically achieved by coating with low-surface-energy materials such as fluoropolymers (Hoshian et al. 2015), silane-based treatments (e.g., fluorosilanes or chlorosilanes) (Brehm et al. 2020), or polydimethylsiloxane (PDMS) (Liu et al. 2019). Self-assembled monolayers (SAMs), prepared by dip-coating (Schondelmaier et al. 2002) or vapor-phase deposition (Chen et al. 2011), enable controlled molecular organization using fluorinated or long-chain alkyl molecules to produce uniform and stable hydrophobic surfaces, while radio-frequency magnetron

sputtering and catalytic chemical vapor deposition (Cat-CVD) can produce durable low-wettability films (Kim et al. 2013). In practice, combining hierarchical roughness with low surface energy modification is an effective route to achieve lotus-leaf-like superhydrophobicity with self-cleaning and low-adhesion characteristics (Hooda et al. 2020). Additional processes, including electrodeposition (Liu et al. 2020) and sol–gel methods (Hsieh et al. 2005), further extend hydrophobic surface treatments to a broad range of substrates, particularly metals and semiconductors.

In recent years, hydrophilic/hydrophobic cooperative (biphasic) surfaces have attracted considerable attention. By patterning regions of distinct surface energy on a single substrate—often in combination with micro-/nanoscale texturing—such surfaces can improve liquid drainage and anti-wetting performance while enabling unconventional interfacial behaviors, with emerging relevance to applications such as pool boiling cooling for AI servers (Onoe et al. 2004). The functional complementarity between domains of contrasting wettability further expands design flexibility in surface engineering and interfacial science. Classical wetting theory based on Young's equation (Young 1805) is generally insufficient for rough or chemically heterogeneous surfaces; therefore, the Wenzel (Wenzel 1936) and Cassie–Baxter (CB) models (Cassie and Baxter 1944) are commonly employed. The CB model, in particular, accounts for

heterogeneity by relating apparent wettability to the fractional contributions of distinct surface domains. Drelich et al. further refined the CB framework by introducing a hemispherical representation of the three-phase contact line and validated the approach using contact-printing experiments (Drelich and Miller 1993; Drelich 1999). They also quantified contact-line line tension via micro-needle gas injection, reporting values on the order of 10^{-12}–10^{-8} J/m (Drelich et al. 1996). Nevertheless, these models and extensions do not fully capture experimentally observed interfacial dynamics on complex biphasic surfaces, highlighting the need for continued mechanistic studies and targeted experimental validation.

Biphasic cooperative surfaces integrate two distinct physicochemical domains on a single substrate and can display nonclassical wetting behavior arising from interfacial coupling. For example, alternating hydrophilic recesses and hydrophobic protrusions can effectively trap air beneath droplets, forming a stable air cushion, thereby increasing apparent hydrophobicity and reducing adhesion (Jung et al. 2005). In high–heat-flux applications (e.g., insulated gate bipolar transistors (IGBTs) modules and high-power laser cooling), hydrophilic/hydrophobic patterning has also been shown to improve boiling performance and heat transfer (Ateş et al. 2023). However, mechanistic understanding of wetting in such biphasic systems remains limited. In this study, well-

defined biphasic substrates were fabricated using photolithography, chemical vapor deposition (CVD), and reactive ion etching (RIE). By systematically varying hydrophobic area fraction, surface roughness, and surface energy, we evaluate their effects on contact angle and wetting state, with the goal of elucidating microscale wetting mechanisms and informing the design of self-cleaning surfaces, antifouling coatings, and high-efficiency thermal interfaces.

2. Experimental Methods

In this study, photolithography, chemical vapor deposition (CVD), and reactive ion etching (RIE) were employed to fabricate biphasic substrates featuring alternating hydrophilic/hydrophobic patterns. The designed patterns consisted of square arrays with side lengths of 10 μm and 40 μm, and the hydrophobic area coverage was adjusted to 25%, 50%, and 75%. Three types of biphasic surface structures were fabricated as follows:(1). SiO_2/FT-SAM biphasic substrate: This substrate consisted of flat, hydrophilic silicon dioxide (SiO_2) regions and hydrophobic square regions. The hydrophobic regions were formed via self-assembled monolayers (SAMs) by covalently grafting perfluorodecyltrichlorosilane (F13-TCS)—abbreviated as FT-SAM—onto the SiO_2 squares, producing a low surface energy layer. This structure is illustrated in Figure 1(a) and Figure 1(c). (2). SiO_2/SiO_2* biphasic substrate: In this structure, the hydrophilic regions remained as flat SiO_2 surfaces, while the hydrophobic square regions (SiO_2* surfaces) were created by RIE treatment, resulting in micro-/nanoscale surface roughness. This configuration is shown in Figure 1(b) and Figure

1(d). (3). SiO_2/SiO_2*-FT-SAM biphasic substrate: Based on the second structure, this configuration involved an additional surface modification step where F13-TCS molecules were covalently bonded to the roughened SiO_2* square regions. This resulted in hydrophobic regions with combined surface roughness and low surface energy, forming a dual-function hydrophobic zone. The hydrophilic regions remained as flat SiO_2, creating a biphasic surface with synergistic hydrophobic effects.

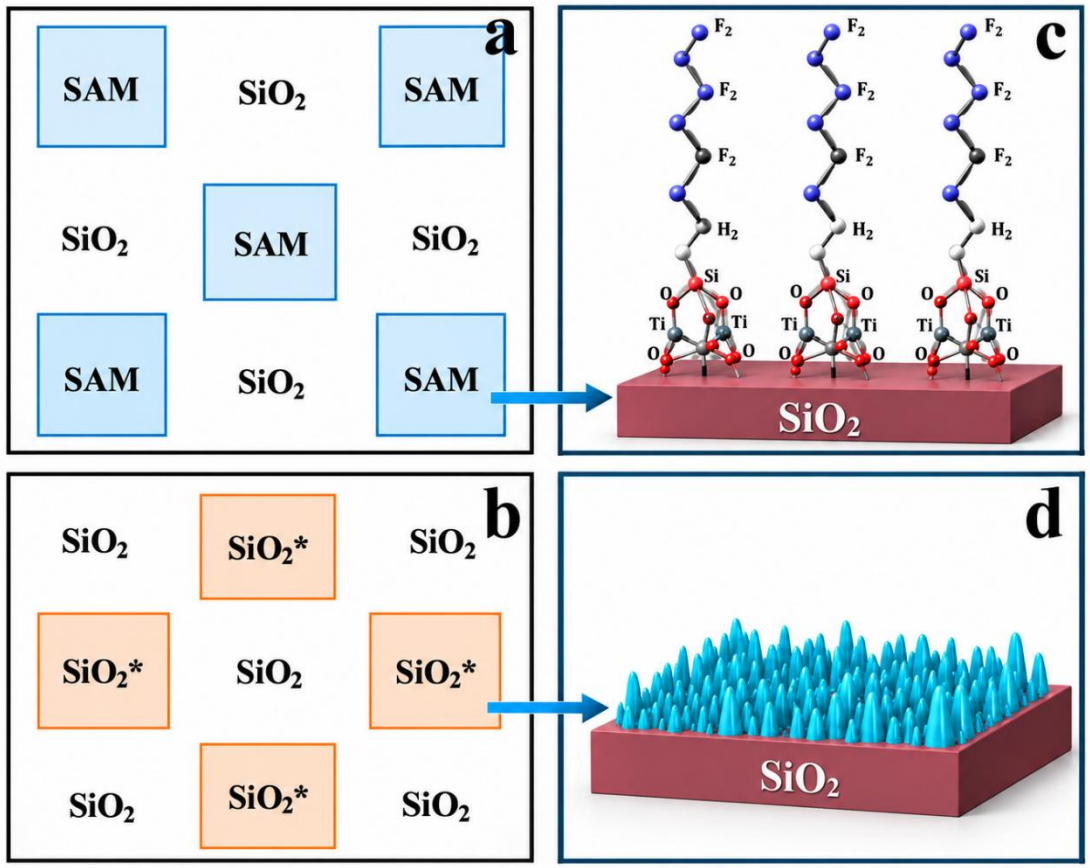


Figure 1. Schematic illustrations of different biphasic substrate structures and surface modifications:(a) SiO_2/FT-SAM biphasic substrate;(b) SiO_2/SiO_2* biphasic substrate. (c) Covalent bonding between F13-TCS molecules and SiO_2 surface forming a self-assembled monolayer (SAM);(d) Surface texture schematic of roughened SiO_2* after

RIE treatment.

2.1 Fabrication of SiO_2/FT-SAM Biphasic Substrate

In this study, a SiO_2/FT-SAM biphasic substrate was fabricated by combining photolithography, chemical vapor deposition (CVD), and self-assembled monolayers (SAMs) techniques. The substrate consisted of hydrophilic silicon dioxide (SiO_2) regions and hydrophobic square-patterned SiO_2 regions modified with F13-TCS [Trichloro(1H,1H,2H,2H-perfluorooctyl) silane], as shown in Figure 1(a). The surface design featured square arrays with side lengths of 10 μm and 40 μm, and the hydrophobic area coverage was controlled at 25%, 50%, and 75% to investigate the influence of geometric parameters on wettability. The fabrication process involved the following steps:(1). Photomask Design and Pattern Definition: A Cr/glass photomask was used to define square array patterns with varying sizes (10 μm and 40 μm) and hydrophobic area coverages (25%, 50%, 75%) to generate the desired micro-patterns on the substrate surface. (2). Substrate Cleaning and Thermal Oxidation: Single-crystal silicon wafers were cleaned using a piranha solution (75% H_2SO_4 : 25% H_2O_2) to remove organic and metallic contaminants, followed by thorough rinsing with deionized (DI) water. The wafers were then subjected to wet thermal oxidation to grow a ~100 nm thick hydrophilic SiO_2 layer on the surface. (3). Photoresist Coating and UV Exposure: A positive photoresist (EPG-512) was spin-coated to a thickness of ~1 μm. After soft baking, the samples were exposed to UV light through the photomask. This was followed by hard baking to stabilize the developed pattern. (4). Development and Pattern Formation: The exposed photoresist areas were developed using a 3% NaOH solution, revealing the underlying SiO_2 in the patterned regions. The substrates were

thoroughly rinsed with DI water. (5). Hydroxylation Treatment: The patterned substrates were placed in an environment with approximately 80% relative humidity to generate surface hydroxyl groups on the exposed SiO_2 regions, facilitating subsequent silane coupling reactions. (6). F13-TCS Modification (SAM Formation): The substrates were placed in a CVD reaction chamber (see Figure 2), preheated to 60°C, and evacuated to 10^{-2} torr to remove moisture. Volatile F13-TCS vapor was then introduced, allowing covalent bonding between F13-TCS molecules and the hydroxylated SiO_2 surface, forming a hydrophobic SAM layer, as illustrated in Figure 1(c). (7). Photoresist Removal and Final Cleaning: Residual photoresist was removed using a 2.38% TMAH solution, followed by ultrasonic cleaning in fresh acetone for 40 min to remove residual unreacted F13-TCS and loosely adsorbed organic byproducts. The substrates were subsequently dried under a nitrogen stream, yielding the SiO_2/FT-SAM biphasic substrate.

The deposition of F13-TCS was carried out using a custom-built chemical vapor deposition (CVD) system, schematically illustrated in Figure 2. The system comprises two main components: a reaction chamber for substrate treatment (left side) and a heating flask (vial) for vaporizing the silane precursor (right side). After the hydroxylation treatment (Step 5), the patterned substrate was placed in the left reaction chamber. The chamber was first heated to 60 °C and evacuated to a pressure of 10^{-2} torr for 1 hour to thoroughly remove any residual moisture from the substrate and internal surfaces, ensuring stability during the subsequent silanization process. The detailed procedure is as follows:(1). Preconditioning of the Vaporizing Flask: A syringe was inserted into the inlet port of the vaporizing flask (right side of Figure 2). Air was first expelled from the flask, and an O-ring was used to seal the inlet, ensuring airtightness.

The F13-TCS inlet valve and the vacuum valve of the reaction chamber were then opened to further remove any residual moisture in the system. (2). Preheating and Vaporization of F13-TCS: The base of the vaporizing flask was heated to 210 °C and maintained under vacuum (~10^{-2} torr) for 30 minutes to achieve thermal equilibrium, completing the system preconditioning. (3). F13-TCS Introduction and Vapor Diffusion: After preheating, both the F13-TCS inlet valve and the reaction chamber vacuum valve were closed to isolate the chamber. A clean syringe was used to withdraw 0.2 mL of F13-TCS, which was then re-injected into the inlet of the vaporizing flask. To avoid pressure surges that might displace the substrate, the vacuum pump valve was first closed, and the F13-TCS inlet valve was slowly opened. Under high temperature (210 °C) and low pressure (10^{-2} torr), the F13-TCS began to vaporize and gradually diffuse into the reaction chamber. (4). Formation of Self-Assembled Monolayer (SAM): After approximately 5 minutes of F13-TCS vapor diffusion, a covalently bonded SAM layer spontaneously formed on the SiO_2 surface via reaction with surface hydroxyl groups, rendering the surface hydrophobic, as illustrated in Figure 1(c).

Upon completion of the reaction, the vacuum valve was reopened to purge residual vapors and byproducts. The chamber was then vented and opened. (5). Post-Cleaning and Drying: To remove byproducts (e.g., HCl) and unreacted F13-TCS molecules, acetone was sprayed evenly over the substrate surface until fully wetted. The substrate was then immersed in fresh acetone and ultrasonically cleaned for 1 minute. Finally, the sample was dried using high-purity nitrogen gas, completing the SAM deposition process.

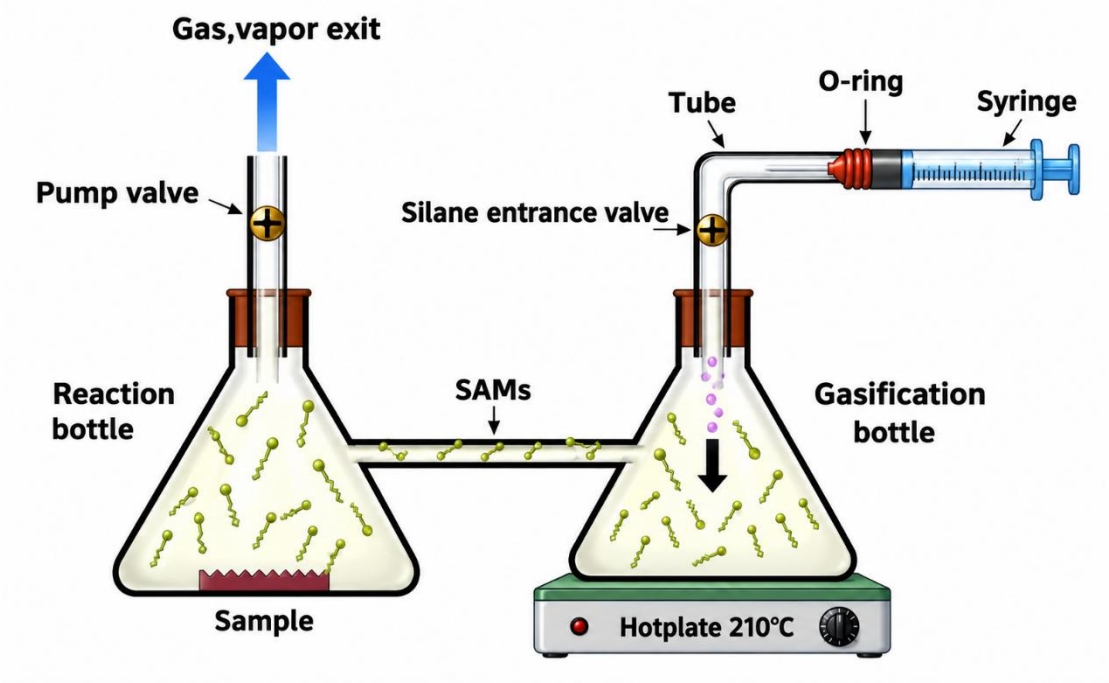


Figure 2. Schematic illustration of the chemical vapor deposition (CVD) system for F13-TCS deposition. The system consists of a reaction chamber (left) for substrate processing and a heating flask (right) for vaporizing the F13-TCS precursor.

2.2 Fabrication of SiO_2/SiO_2* Biphasic Substrates

The SiO_2/SiO_2* biphasic substrate consists of hydrophilic silicon dioxide (SiO_2) regions and hydrophobic square-patterned SiO_2* regions, which are formed by reactive ion etching (RIE) to introduce micro/nanoscale hierarchical surface roughness. A schematic of the structure is shown in Figure 1(b). The surface pattern comprises an array of alternating hydrophilic and hydrophobic square regions with varying side lengths (10 μm and 40 μm) and hydrophobic area coverages (25%, 50%, and 75%). The initial four fabrication steps are identical to those used for the SiO_2/FT-SAM biphasic substrate. The subsequent process steps are as follows:(5) Dry Etching (RIE): Reactive ion etching is performed on the pre-defined exposed square areas designated as the hydrophobic regions, to roughen the SiO_2 surface and form SiO_2*. A gas mixture of CF_4

and O_2 is used as the etchant, with the etching rate controlled at approximately 30–40 Å/min. With optimized etching duration, hierarchical structures with multi-scale micro/nanoscale roughness are formed, resulting in an average root mean square (RMS) surface roughness of approximately 100 nm. This hierarchical roughness effectively reduces the real contact area with water and enhances the surface hydrophobicity. (6) Photoresist Removal and Surface Cleaning: Following the RIE process, residual photoresist is removed using a 2.38% TMAH alkaline solution. The substrates are then immersed in fresh acetone and cleaned via ultrasonic agitation for 40 minutes to remove etching residues and particles. Finally, the substrates are dried using high-purity nitrogen gas, completing the fabrication of the SiO_2/SiO_2* biphasic substrate.

2.3 Fabrication of SiO_2/SiO_2*-FT-SAM Biphasic Substrates

The SiO_2/SiO_2*-FT-SAM biphasic substrate consists of hydrophilic silicon dioxide (SiO_2) regions and hydrophobic regions composed of SiO_2* surfaces with micro/nanoscale roughness generated via reactive ion etching (RIE), followed by covalent grafting of low surface energy fluorosilane molecules (F13-TCS) to form a self-assembled monolayer (SAM). The initial four fabrication steps are the same as those for the SiO_2/FT-SAM biphasic substrates. The subsequent process is as follows:(5) Dry Etching (RIE): Selective reactive ion etching is performed on the patterned regions designated for the hydrophobic phase. Under controlled etching conditions, a mixture of CF_4 and O_2 gases is used to etch the SiO_2 surface at a rate of approximately 30–40 Å/min, resulting in a hierarchical micro/nanostructured SiO_2* surface. The average root mean square (RMS) roughness reaches approximately 100 nm, which provides increased surface roughness favorable for enhancing hydrophobic performance. (6)

Hydroxylation Treatment: The etched substrate is placed in a high-humidity environment (approximately 80% relative humidity) to promote the formation of hydroxyl groups on both the flat SiO_2 and roughened SiO_2* surfaces. These hydroxyl groups serve as active sites for subsequent covalent bonding with F13-TCS molecules. (7) F13-TCS Modification (SAM Deposition): The hydroxylated substrate is placed into a custom-built chemical vapor deposition (CVD) system for self-assembled monolayer (SAM) modification using F13-TCS. The reaction chamber is preheated to 60 °C and evacuated to 10^{-2} torr to remove residual moisture. Volatilized F13-TCS vapor, heated to 210 °C, is then introduced and reacts with the surface hydroxyl groups on both SiO_2 and SiO_2*, forming a stable, covalently bonded, hydrophobic SAM layer. (8) Photoresist Removal and Final Cleaning: After SAM formation, the residual photoresist is removed using a 2.38% TMAH alkaline solution. The substrate is then immersed in fresh acetone and ultrasonically cleaned for 40 minutes to remove any unreacted F13-TCS molecules and reaction by-products. Finally, the substrate is dried with high-purity nitrogen gas, completing the fabrication of the SiO_2/SiO_2*-FT-SAM biphasic substrate.

2.4 Fabrication of Large-Area Hydrophobic Thin Films

Considering the limitations of traditional photolithography, chemical vapor deposition (CVD), and reactive ion etching (RIE) in terms of equipment cost and scalability, these processes are not ideal for the fabrication of large-area hydrophobic thin films. In this study, we propose a scalable fabrication strategy that combines microstructure design with the synergistic effect of low surface energy molecules to realize large-area hydrophobic coatings. A polyethylene terephthalate (PET) film, pre-

treated with a surface primer and sized at 30 cm × 30 cm × 250 μm, was used as the substrate. A layer of UV-curable acrylic resin, with a peak photosensitivity at 365 nm, was spin-coated onto the surface. To impart hydrophobicity, 1 wt% of bifunctional polydimethylsiloxane acrylate (PDMS acrylate, molecular weight ~2000 g/mol) was added to the resin formulation. Due to its excellent surface migration properties, the PDMS molecules spontaneously accumulate at the surface during the UV curing and crosslinking process, forming a stable hydrophobic layer with low surface energy. To improve the dispersion and stability of PDMS in the UV resin matrix, propylene glycol monomethyl ether acetate (PGMEA) was used as a compatibilizing solvent. PDMS and PGMEA were pre-mixed at a 1:1 weight ratio and stirred with a magnetic stirrer for 15 minutes to ensure uniform blending. The mixture was then slowly added to the UV resin base and stirred again for homogeneity. After mixing, the solution was degassed in a vacuum chamber (10^{-2} torr) to remove air bubbles introduced during mixing, ensuring coating uniformity and curing quality. The coated samples were preheated in a 180 °C oven for 10 minutes to completely evaporate the PGMEA solvent. After cooling, the samples were transferred to a controlled darkroom (temperature: 21 °C, relative humidity: 60%) for pre-treatment. To investigate the influence of ambient humidity and dew point on the final hydrophobic surface formation, two curing conditions were designed:(1). Sample 1: Direct UV curing under a relative humidity of 60%. (2). Sample 2: Pre-conditioned by placing the sample in an environment with a dew point of 16 °C for 1 minute, then transferred to an 18 °C environment for another minute, followed by UV curing at a relative humidity of 70%. Both samples were cured using an 8 W UV mercury lamp for 1 hour to ensure complete crosslinking of the UV resin, resulting in mechanically stable and hydrophobic thin films.

2.5 Surface Morphology and Wettability Characterization Methods

To comprehensively evaluate the surface morphology, roughness, and wetting behavior of the dual-phase substrates, the following experimental measurements and characterization techniques were employed:(1). Surface Roughness Measurement To analyze the micro-regional surface topography and roughness of the dual-phase substrates, an atomic force microscope (AFM; SEIKO SPI3800N) was used to perform high-resolution scans, providing nanoscale surface height variation data. In addition, to complement the limited coverage of micro-scale measurements, a surface profilometer (KLA-Tencor Alpha-Step 500) was employed to perform large-area height scanning. This allowed for the acquisition of overall roughness (Root Mean Square, RMS) and surface flatness parameters, enabling a comprehensive understanding of surface characteristics across both micro- and macro-scales. (2). Microscale Structural Observation: The surface microstructures of the substrates were analyzed using a scanning electron microscope (SEM; Hitachi S-2600H). Although SEM imaging typically requires metal coating for non-conductive samples, no conductive coating was applied in this study. This was due to the inherent contrast generated by the conductivity difference between hydrophilic and hydrophobic regions, which enabled clear visualization of the dual-phase patterns. Furthermore, an additional AFM system (Digital Instruments D3000) was utilized to supplement the structural analysis and improve resolution and verification of features within roughened regions. (3). Contact Angle Measurement: To assess the wettability of different surface regions, static contact angle measurements were conducted using a vertical contact angle analyzer (FTA-125, First Ten Angstrom). All measurements were performed under controlled environmental conditions: temperature maintained at 25 °C and relative humidity at 50–

60%. Two volumes of deionized water droplets, 1.8 μL and 6.6 μL, were used as probe liquids. For each sample, six repeated measurements were taken at specified locations, and the average value was used as the representative contact angle for that region. The dual-volume approach was adopted to examine the sensitivity of contact angles to droplet size, thereby enhancing the accuracy and reproducibility of the results.

3.Results and Discussion

3.1 Microstructural and Wettability Analysis of SiO_2/FT-SAM Dual-Phase Substrates

To fabricate dual-phase substrates featuring alternating hydrophilic and hydrophobic regions, this study first employed photolithography to define square array patterns. Upon UV exposure, the positive photoresist (EPG-512) underwent photodecomposition in the transparent regions of the photomask. The exposed areas were then developed using EDP-1000 developer, revealing the underlying hydrophilic SiO_2 surface. In contrast, the unexposed regions remained protected by the photoresist, preserving their original properties. This patterning process created reaction windows for subsequent selective self-assembly. Next, a chemical vapor deposition (CVD) process was conducted to deposit the low-surface-energy fluorosilane precursor F13-TCS. Under controlled temperature and vacuum conditions, the vaporized F13-TCS molecules reacted covalently with hydroxyl groups present on the exposed SiO_2 surface, forming a self-assembled monolayer (SAM). Finally, residual photoresist was removed using an alkaline solution, yielding a dual-phase substrate comprising hydrophobic FT-SAM and hydrophilic SiO_2 regions arranged in an alternating pattern. Under various geometric configurations (square side lengths of 10 μm and 40 μm; FT-SAM coverage ratios of

25%, 50%, and 75%), the resulting surface microstructures were characterized using electron microscopy (SEM), as shown in Figure 3. In the SEM images, the brighter regions correspond to the hydrophilic SiO_2 areas not covered by FT-SAM, while the darker regions indicate the hydrophobic areas coated with F13-TCS molecules. The strong contrast enables clear identification of the spatial distribution of the dual-phase pattern, confirming high pattern fidelity and process uniformity.

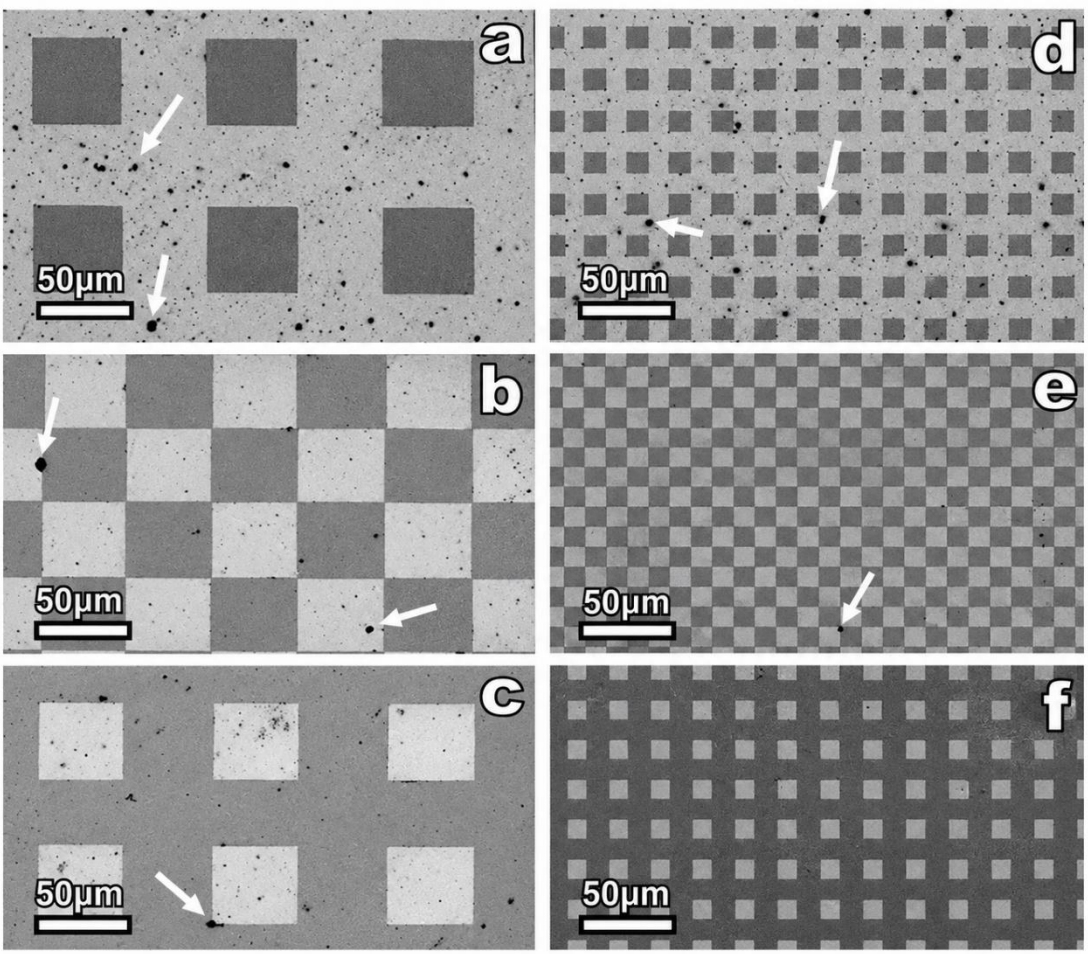


Figure 3. Scanning electron microscopy (SEM) images of SiO_2/FT-SAM dual-phase substrates with varying design parameters. Bright regions correspond to hydrophilic SiO_2, while dark regions indicate hydrophobic FT-SAM-coated areas. White arrows

highlight areas where F13-TCS molecules have aggregated. Images: (a–c) 40 μm square patterns with FT-SAM coverage of 25%, 50%, and 75%, respectively; (d–f) 10 μm square patterns with FT-SAM coverage of 25%, 50%, and 75%, respectively.

To further validate the physical property differences and boundary precision between hydrophilic and hydrophobic regions, frictional force mode atomic force microscopy (AFM) was employed, with results shown in Figure 4. The sample with 25% FT-SAM coverage exhibited clear contrast in lateral force signals between the two regions, demonstrating highly selective SAM deposition confined to designated areas. The sharp boundaries and absence of diffusion artifacts indicate excellent chemical patterning resolution and surface selectivity.

To comprehensively evaluate the surface roughness and planarity of the SiO_2/FT-SAM dual-phase substrates, a multi-scale surface topography analysis was conducted using both Atomic Force Microscopy (AFM; SEIKO SPI3800N) and a surface profilometer (KLA-Tencor Alpha-Step 500). Table 1 summarizes the root mean square (RMS) roughness values of the dual-phase substrates under various geometric conditions, including square sizes of 10 μm and 40 μm, and FT-SAM coverage ratios of 25%, 50%, and 75%. A representative three-dimensional AFM topographic image of the substrate with 40 μm squares and 50% FT-SAM coverage is shown in Figure 5. The measurement results indicate that both the hydrophilic SiO_2 regions and the hydrophobic FT-SAM regions exhibit RMS roughness values below 5 nm, confirming that the deposition of F13-TCS via self-assembled monolayer (SAM) formation does not significantly alter the underlying surface morphology. Although slightly increased roughness was observed in localized areas for samples with 10 μm square patterns, the values remain within the nanometer scale, and the overall surface remains highly planar,

ensuring negligible height difference across the dual-phase interfaces.

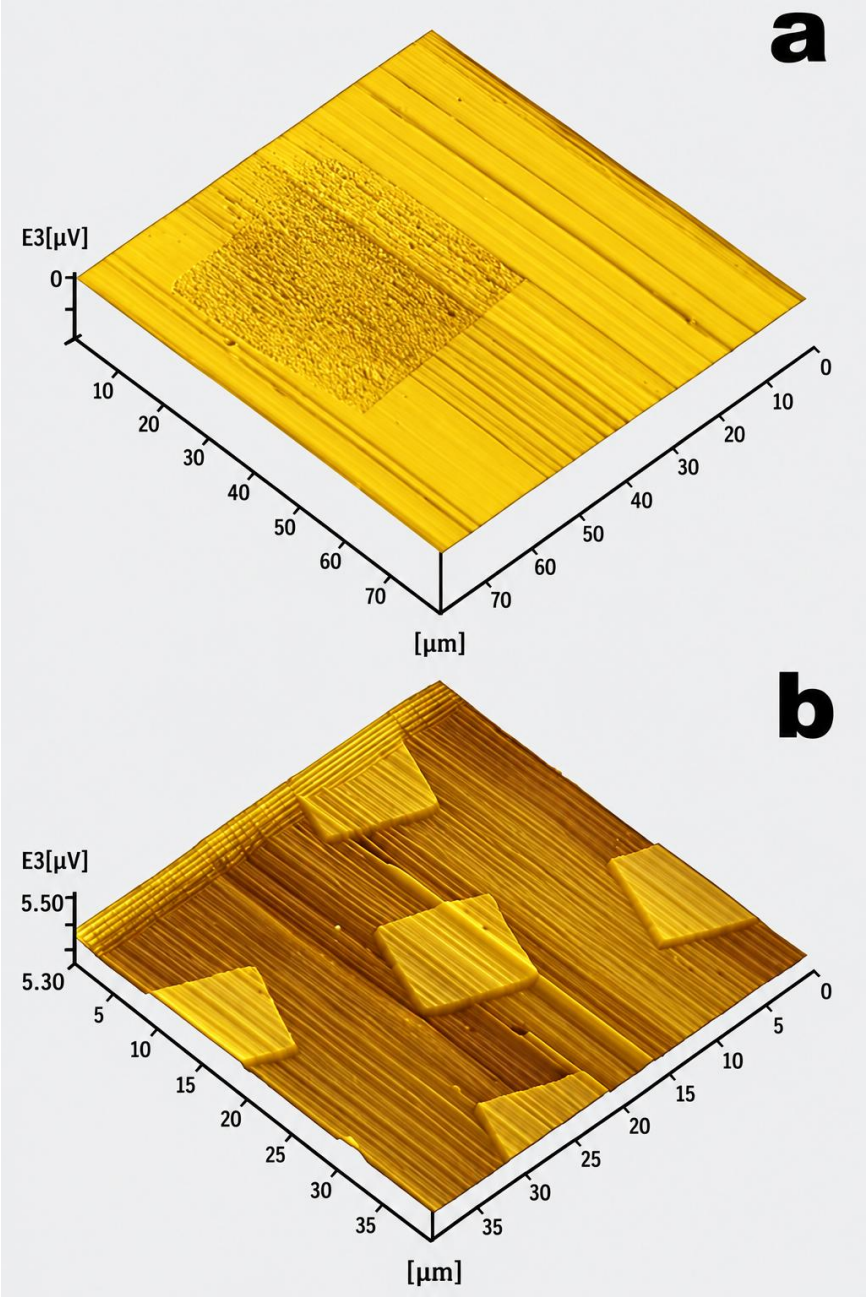


Figure 4. Atomic force microscopy (AFM) friction force images of SiO_2/FT-SAM dual-phase substrates with 25% FT-SAM coverage. (a) 40 µm square pattern; (b) 10 µm square pattern. Clear friction contrast indicates well-defined boundaries between hydrophilic and hydrophobic regions.

To further verify substrate coplanarity on a larger scale, high-precision linear scans were performed using the α-step profilometer along a 45° diagonal direction across the substrate. The scan parameters were set to a length of 500 μm and a scan rate of 50 μm/s, and measurements were repeated at five distinct locations to ensure statistical robustness. As shown in Figure 5, the height variation across the boundary between hydrophilic and hydrophobic regions is minimal, and the average RMS roughness of the dual-phase substrates is comparable to that of pure SiO_2 and fully FT-SAM-coated substrates. These results confirm that the fabricated SiO_2/FT-SAM dual-phase substrates are essentially coplanar structures, and the wettability contrast arises primarily from variations in surface chemical energy, rather than from topographical features. This characteristic is critical for accurate contact angle measurements and wetting behavior analysis, particularly when applying theoretical models such as Cassie–Baxter and Wenzel. The near-coplanar nature of the surface minimizes wetting artifacts induced by height discontinuities, thereby enhancing the reliability and interpretability of droplet behavior observations.。

Table 1. Average surface roughness (Root Mean Square, RMS, in nm) of SiO_2/FT-SAM dual-phase substrates measured by AFM under different FT-SAM coverage ratios and pattern sizes (10 μm and 40 μm squares).

RMS(nm) / SAM (%)	SiO_2 line profile		F_{13}-TCS SAM line profile	
	10μm	40μm	10μm	40μm
25	1.4	0.1	2.2	0.2

50	0.8	0.2	1.6	0.4
75	3.4	0.1	4.7	0.2

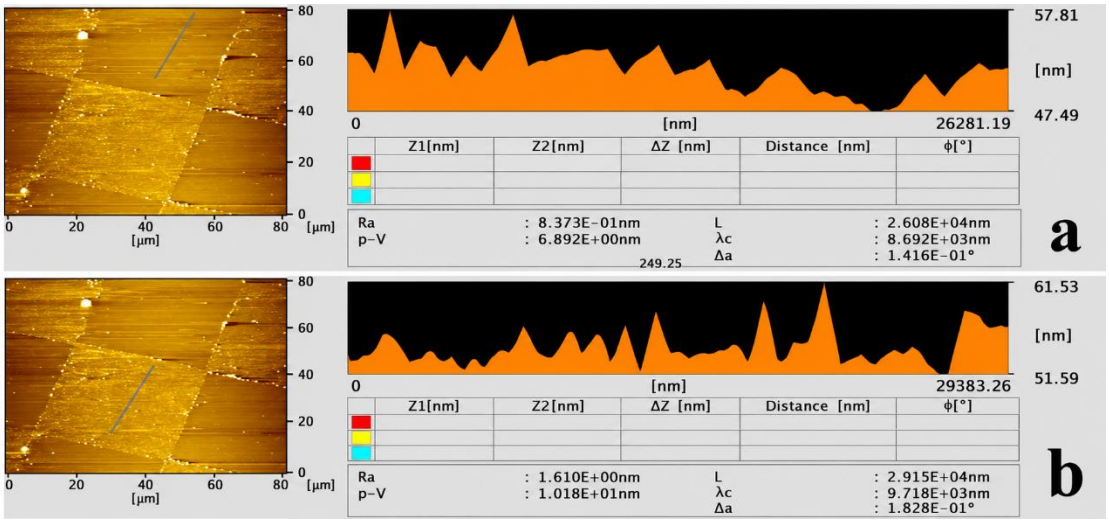


Figure 5. AFM analysis of SiO_2/FT-SAM dual-phase substrate with 50% FT-SAM coverage and 40 μm square pattern:(a) morphology and roughness profile of the hydrophilic SiO_2 region; (b) morphology and roughness profile of the hydrophobic F13-TCS region.

Table 2 and Figure 6 present the effects of different water droplet volumes (1.8 μL and 6.6 μL), square pattern sizes (10 μm and 40 μm), and FT-SAM coverage ratios (25%, 75%, and 100%) on the static contact angles of SiO_2/FT-SAM biphasic substrates. The results show that as the FT-SAM coverage increases from 0% to approximately 50%, the contact angle significantly increases; however, when the coverage exceeds 50%, the increase in contact angle slows down and gradually saturates. This phenomenon can be explained by the Cassie–Baxter model, expressed as $\cos\theta_{CB} = f1\cos\theta1 + f2\cos\theta2$, where f1 and f2 are the area fractions of the hydrophilic SiO_2 and hydrophobic FT-SAM regions, respectively, and θ1 and θ2 are their corresponding contact angles. As the

hydrophobic fraction f2 increases, the droplet interface is increasingly covered by the low surface energy FT-SAM regions, resulting in a significant increase in the overall contact angle. When the coverage exceeds 50%, the droplet contact line mainly lies on the hydrophobic area, and the influence of the hydrophilic region diminishes, causing the contact angle to increase to plateau. This reflects a wetting behavior transition from "biphasic wetting dominance" to "hydrophobic single-phase dominance," demonstrating a clear wetting phase transition.

Furthermore, the droplet volume also has a significant effect on the contact angle. In samples with high coverage (≥50%), smaller droplets (1.8 μL) generally exhibit larger contact angles compared to larger droplets (6.6 μL). This phenomenon is primarily attributed to gravitational effects on the shape of larger droplets, which tend to spread more easily, reducing the contact angle. Conversely, smaller droplets are dominated by surface tension and maintain a shape closer to a sphere. This mechanism can be described by the Bond number (Bo), defined as $Bo = \rho g R^2/\gamma$, where ρ is the density of water, g is gravitational acceleration, R is the droplet radius, and γ is the surface tension of water. As the droplet radius R increases, gravitational effects become more pronounced, causing droplets to flatten and decreasing the contact angle. In contrast, for samples with low coverage (0% and 25%), the surface is more hydrophilic, and the droplet size has a limited effect on the contact angle, indicating that the wetting behavior is primarily governed by surface chemical properties rather than gravitational effects. These results further confirm the wetting property variation mechanism of biphasic substrates and provide important guidance for the design of functional surfaces with specific wetting behaviors.。

Table 2. Comparison of the average static contact angles of SiO_2/FT-SAM biphasic

substrates under different water droplet volumes and FT-SAM coverage ratios. Small droplets (SD) have a volume of 1.8 μL, and large droplets (LD) have a volume of 6.6 μL.

side length / FT-SAM (%)	Contact angle (°)			
	10μm		40μm	
	SD	LD	SD	LD
100	103	95	107	97
75	103	94	107	97
50	102	94	106	98
25	82	80	83	82
0	62	62	62	62

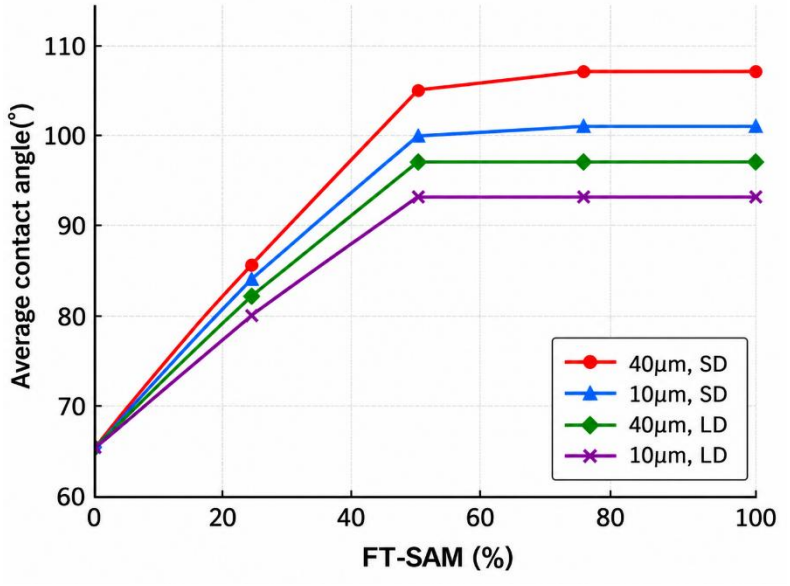


Figure 6. Relationship between the average contact angle (C.A.) of SiO_2/FT-SAM biphasic substrates and the apparent surface area ratio of SAM, measured using water droplets of different volumes: small droplets (SD) at 1.8 μL and large droplets (LD) at 6.6 μL.

Additionally, the three-phase contact line of droplets on the heterogeneous SiO_2/FT-SAM biphasic substrate exhibits pronounced asymmetry and localized distortion, as shown in Figure 7. This phenomenon primarily arises from the significant difference in surface free energy between the hydrophilic SiO_2 and hydrophobic FT-SAM regions, causing the droplet's contact line to become pinned at the heterogenous interface, resulting in contact angle hysteresis effects. As the droplet overcomes the energy barrier, it must continuously adjust its local shape to maintain mechanical equilibrium, forming a non-circular and asymmetric contour. Compared to homogeneous surfaces, the biphasic substrate displays more complex contact line dynamics, reflecting notable energy barriers and uneven distribution of interfacial tension during the wetting process.

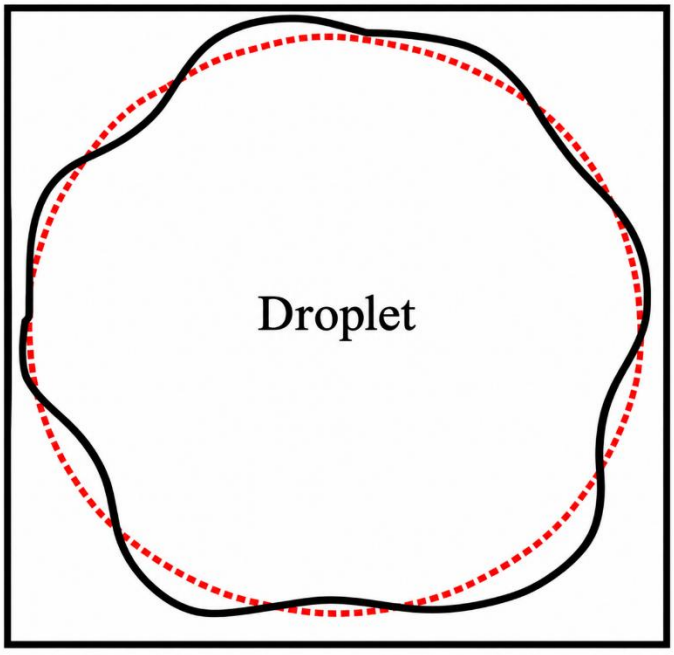


Figure 7. Schematic illustration of liquid wetting behavior on the SiO_2/FT-SAM biphasic substrate (top view). The dashed line represents the symmetric circular contact line of a droplet on an ideal homogeneous surface, while the solid line shows the asymmetric and locally distorted contact line of a droplet on the biphasic heterogeneous

surface.

As shown in Table 3, the static contact angle of the pure SiO_2 substrate without F13-TCS modification (SAM coverage 0%) is approximately 62°, while the substrate fully covered with the SAM (100% coverage) exhibits a significantly increased contact angle of about 103°, clearly confirming that the fluorinated self-assembled monolayer (SAM) modification effectively enhances the hydrophobicity of the substrate surface and provides a stable reference for subsequent wetting behavior analysis of the biphasic substrate. For the SiO_2/FT-SAM biphasic coplanar substrate, when the FT-SAM coverage reaches 50%, the measured contact angles—regardless of whether the pattern size is 10 μm or 40 μm—are close to the contact angle of the pure SAM surface (about 103°). This result indicates that once the hydrophobic area proportion exceeds a certain threshold, the droplet wetting behavior is primarily governed by the hydrophobic phase, with the influence of the hydrophilic SiO_2 region significantly diminished. Furthermore, comparing samples with the same coverage (75%) but different pattern sizes reveal that the contact angle on the 40 μm patterned substrate is generally higher than that of the 10 μm sample. This phenomenon suggests that even under the same coverage ratio, the pattern size still significantly affects wetting behavior. Possible reasons include contact line pinning and distortion effects at the hydrophilic/hydrophobic boundaries, local interfacial energy differences, and contact angle hysteresis and other wetting dynamics factors. Theoretically, the Cassie–Baxter model can be used in a weighted average form to describe the apparent contact angle of the biphasic substrate: $\cos\theta_C=(1-p)\cos62^\circ+p\cos103^\circ$, where p is the SAM coverage ratio, and 62° and 103° are the intrinsic contact angles of SiO_2 and SAM, respectively. From the data in Table 3, the theoretical values generally align well with the experimental results, especially

under high coverage conditions. However, for smaller pattern sizes (10 μm), the measured contact angles are generally higher than the theoretical predictions, reflecting the influence of geometric scale effects and dynamic contact line behavior that cause wetting phenomena to deviate from the ideal assumptions of the classical Cassie–Baxter model. It is worth noting that the Cassie–Baxter model was originally developed to describe superhydrophobic behavior on composite solid-air interfaces of rough surfaces, with the theoretical formula:： $\cos\theta_C=\varphi s\cos\theta+(1-\varphi s)\cos180°$， where ϕs is the solid coverage fraction and θ is the intrinsic contact angle of the solid. The model assumes that wetting behavior is mainly governed by composite interfacial effects induced by surface roughness.

However, the wetting properties of the biphasic substrates prepared in this study are primarily controlled by surface chemical heterogeneity. The droplets on the alternating hydrophilic/hydrophobic regions face significant interfacial energy differences, leading to contact line pinning and non-uniform wetting. This results in the classical Cassie–Baxter model generally underestimating the actual contact angles.

Table 3. Comparison of the average contact angles measured using small droplets on SiO_2/FT-SAM biphasic cooperative substrates at different SAM coverage ratios, showing experimental values and theoretical values calculated by the Cassie–Baxter (CB) model.

FT-SAM (%)	Contact angle (°) (SD)			Contact angle (°) (LD)		
	Cal.(°)	Exp.	Exp.	Cal.(°)	Exp.	Exp.

		10μm	40μm		10μm	40μm
100	103	103	106	95	95	97
75	92	103	107	87	94	97
50	82	102	106	78	94	98
25	72	82	83	70	80	82
0	62	62	62	62	62	62

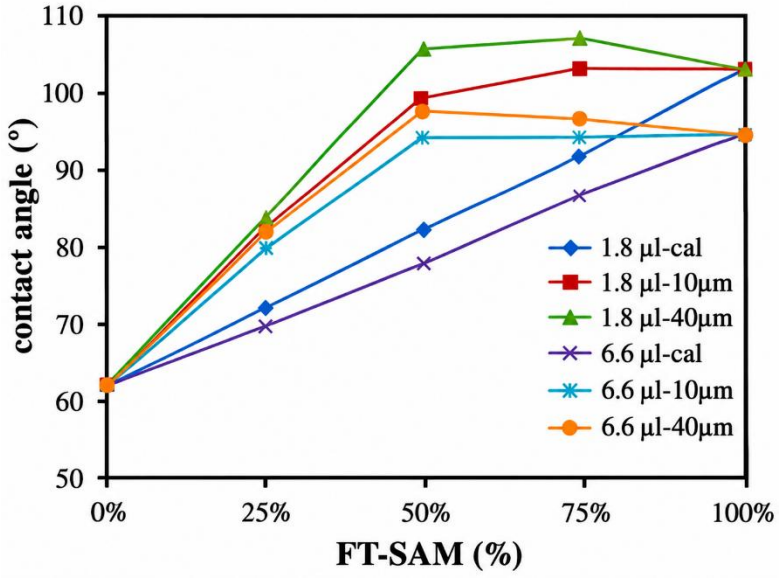


Figure 8. Comparison of average contact angles measured with small droplets (1.8 μL) and large droplets (6.6 μL) on SiO_2/FT-SAM biphasic substrates with varying SAM coverage ratios and pattern sizes (10 μm and 40 μm), showing experimental values and theoretical values predicted by the Cassie–Baxter (CB) model.

Figure 9 illustrates the differences in droplet contact angle profiles and potential trapped air structures on biphasic substrates with varying SiO_2* coverage ratios (25%, 50%, and 75%). At low coverage (25%), distinct stripes and interference fringes appear at the droplet base, as shown in Figures 12(a) and 12(b), indicating localized air cavities between the droplet and substrate, forming discrete closed air entrapment structures.

However, uneven gas distribution leads to droplet profile deformation and unstable wetting behavior. In contrast, at higher coverage ratios (50% and 75%), the droplet profiles become smoother without obvious interference patterns, yet the contact angles significantly increase, suggesting that the air cavities beneath the droplet may transition into a continuous gas interface structure, i.e., a dynamic plastron. It is inferred that as the FT-SAM area fraction increases, the initial droplet contact is rapidly repelled by a large hydrophobic region, forming a stable gas boundary layer at the base, effectively preventing liquid penetration into the solid surface. This annular gas film not only supports the droplet but also substantially enhances wetting repellency. Furthermore, pattern size plays a key role in the gas film behavior. Under the same coverage conditions, substrates with 40 μm patterns generally exhibit higher contact angles than those with 10 μm patterns, possibly because larger unit sizes increase the distance between hydrophilic and hydrophobic boundaries, reducing interference from hydrophilic regions on hydrophobic repulsion, thus promoting gas film formation and maintaining droplet symmetry. Conversely, in the 10 μm pattern, densely arranged hydrophilic areas tend to destabilize the gas film, leading to enhanced wettability.

To verify the dynamic nature of the gas film, a lateral airflow (0.3 mL/s) was applied along the droplet's three-phase contact line. The results showed instantaneous deformation and fluctuations at the droplet base in samples with 50% and 75% coverage, as illustrated in Figures 9(c) and 9(d), indicating transient gas film formation driven by airflow and triggering wetting mode transitions. This phenomenon resembles the air cushion support mechanism observed in the lotus leaf effect, significantly improving droplet mobility and contact angle, reducing surface friction, and demonstrating potential for self-cleaning and microdroplet manipulation applications. However, such

dynamic gas film formation and wetting state transitions extend beyond the applicability of the traditional Cassie–Baxter model. The CB model is based on a static air entrapment assumption and treats wetting modes as fixed states, failing to describe the non-uniform gas layer evolution and wetting transitions occurring during airflow or dynamic repulsion processes. Therefore, for these functional heterogeneous surfaces, there is an urgent need to develop multiphase wetting theoretical models that incorporate gas dynamic evolution and nonequilibrium behaviors at the three-phase contact line, to accurately capture wetting characteristics and guide surface design.

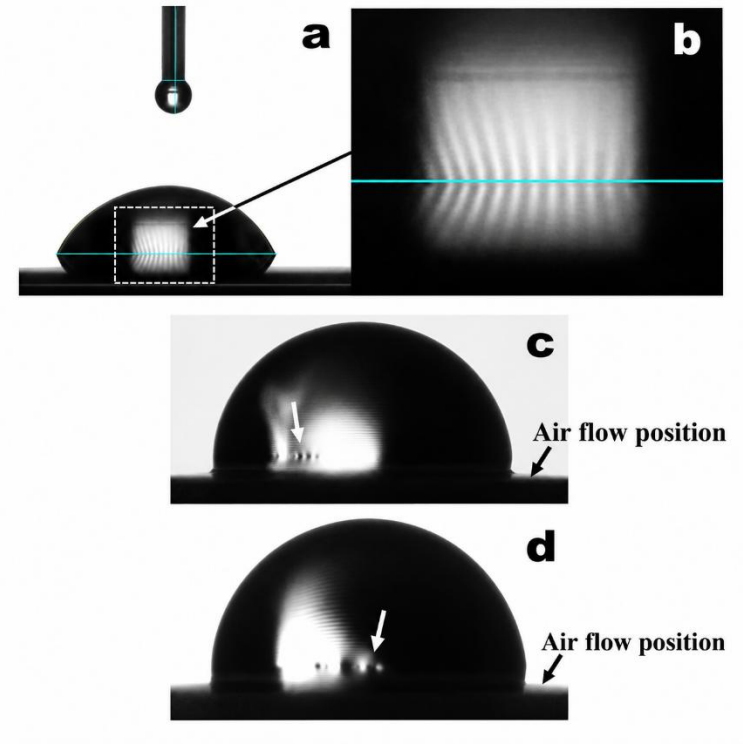


Figure 9. shows dynamic images of water droplet contact angles on biphasic synergistic substrates with self-assembled monolayer (SAM) surface area fractions of (a) 25%; (b) a magnified view of the circled area in (a); (c) 50%; and (d) 75%, with a pattern edge length of 40 μm.

3.2 Microstructure and Contact Angle Analysis of SiO_2/SiO_2 *Biphasic Substrates

In this study, reactive ion etching (RIE) was employed to fabricate biphasic substrates composed of hydrophilic smooth SiO_2 and RIE-roughened SiO_2* without chemical modification (hereafter referred to as SiO_2/SiO_2*). Samples were prepared under different patterning conditions, with square pattern side lengths of 10 μm and 40 μm, and SiO_2* coverage ratios of 25%, 50%, and 75%. Scanning electron microscope (SEM) images of these samples are shown in Figure 10. The images reveal clear and well-defined boundaries for both pattern sizes, demonstrating the high resolution and reproducibility of the lithography process used. To quantify the effect of etching on surface morphology, the thickness change of the thermally grown SiO_2 layer was measured using an α-STEP surface profiler. Results indicate that the oxide thickness decreased from approximately 3498 Å before etching to about 2450 Å after etching, corresponding to an etching depth of roughly 1048 Å—within the submicron scale range. This etching depth may induce significant changes in wetting behavior and is below the critical roughness threshold dominated by capillary pressure, thereby effectively decoupling the influences of roughness and surface chemical energy. This provides an ideal physical biphasic platform for comparative studies.

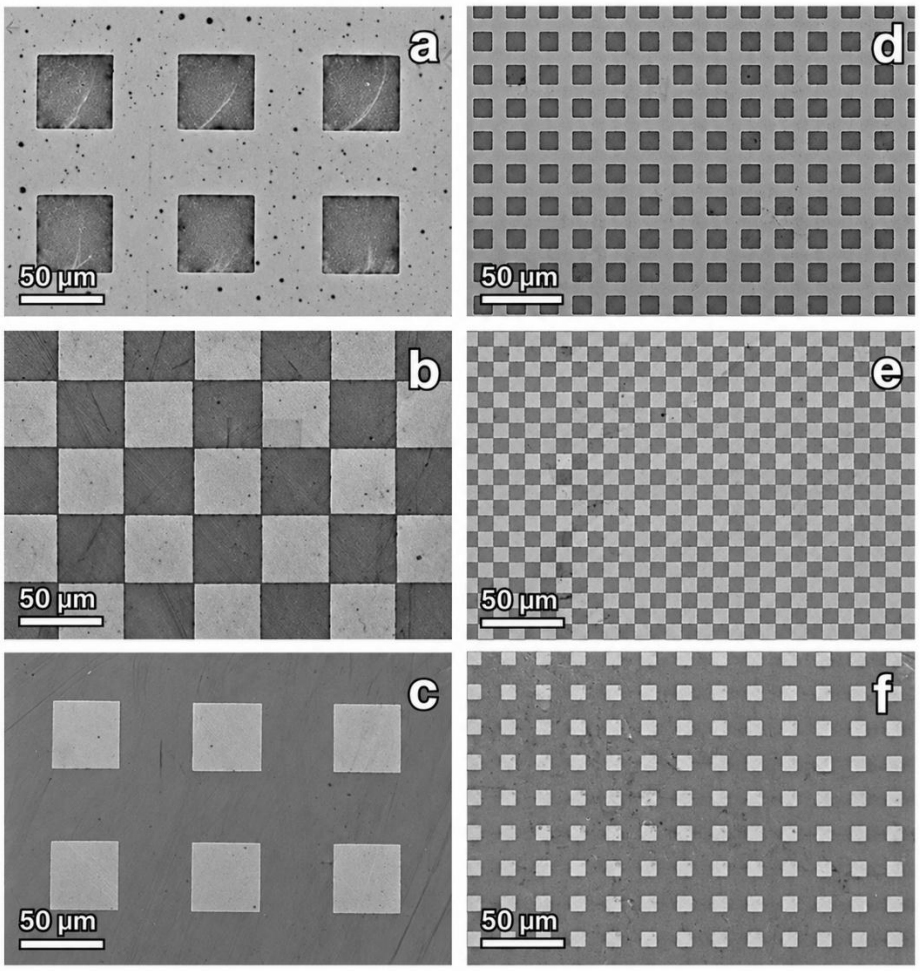


Figure 10. Scanning Electron Microscope (SEM) images of the SiO_2/SiO_2* biphasic substrates. The brighter regions correspond to the unetched smooth SiO_2 areas, while the darker regions represent the roughened SiO_2* microporous arrays formed by reactive ion etching (RIE). (a–c) Pattern side length of 40 μm with air area ratios of 25%, 50%, and 75%, respectively;(d–f) Pattern side length of 10 μm with air area ratios of 25%, 50%, and 75%, respectively.

Table 4 and Figure 11 present the static contact angle measurements of the SiO_2/SiO_2* biphasic substrates under varying square pattern side lengths (10 μm and 40 μm) and droplet volumes (1.8 μL and 6.6 μL). Overall, the measured contact angles for all samples are significantly lower than the theoretical values predicted by the traditional Cassie–Baxter (CB) model, indicating limitations of this model in describing

the wetting behavior on such physically heterogeneous biphasic solid surfaces. Notably, the deviation between theory and experiment is especially pronounced when the pattern size is larger (40 μm) or the droplet volume is smaller (1.8 μL). This phenomenon suggests that the wetting behavior of droplets is not solely governed by the area fraction of the hydrophobic regions but is also strongly influenced by the dynamic effects of the three-phase contact line and the surface topography. Specifically, the three-phase contact line undergoes significant deformation and pinning at the interface between hydrophilic SiO_2 and roughened SiO_2*, combined with local wetting energy barriers and contact angle hysteresis effects. These factors cause the droplet morphology and spreading behavior to deviate from the uniform wetting assumptions inherent in the CB model. Theoretically, the CB model treats the hydrophobic regions as equivalent to ideal air pockets, where the "air cushion effect" leads to higher contact angles. However, in this study, the SiO_2* regions are rough solid surfaces rather than true air cavities. Although this rough structure effectively suppresses liquid penetration and increases wetting energy barriers, the mechanism fundamentally differs from the air-trapping effect in the CB model, resulting in a systematic overestimating of the actual contact angles. This deviation is further amplified at larger pattern scales, where the droplet's three-phase contact line crosses longer heterogeneous interfaces, leading to more pronounced local pinning and energy barriers, thus increasing the discrepancy in contact angles. Table 4 summarizes the average static contact angles of the SiO_2/SiO_2* biphasic substrates under different droplet volumes and SiO_2* coverage ratios. Small droplets (SD) have a volume of 1.8 μL, while large droplets (LD) are 6.6 μL, reflecting the differing influences of gravity and surface tension on wetting behavior at different droplet scales.

Table 4. Comparison of the average static contact angles of SiO_2/SiO_2* biphasic substrates under different droplet volumes and SiO_2* coverage ratios. Small droplets (SD) have a volume of 1.8 μL, and large droplets (LD) have a volume of 6.6 μL.

Side length / SiO_2*(%)	Contact angle (°)			
	10μm		40μm	
	SD	LD	SD	LD
100	72	72	72	72
75	48	47	44	49
50	59	61	55	55
25	67	70	67	65
0	61	61	58	58

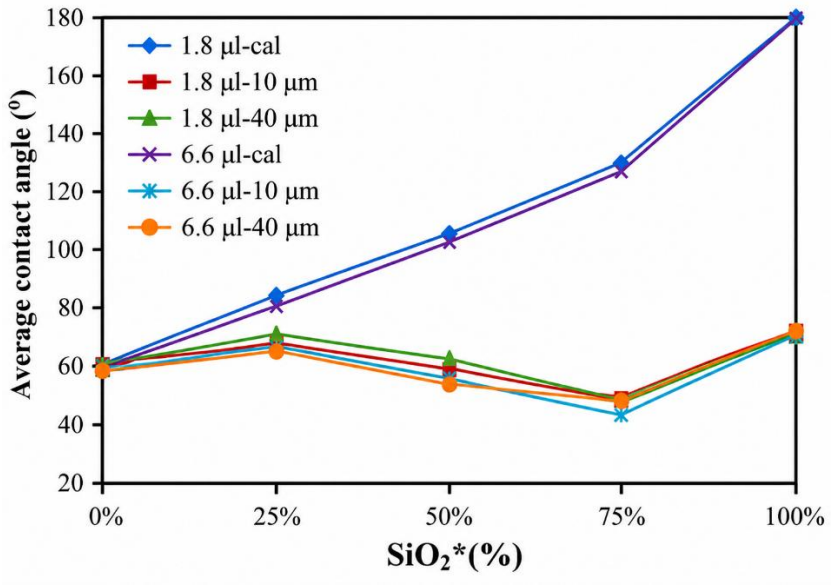


Figure 11. Comparison of the average static contact angles of SiO_2/SiO_2* biphasic substrates under different SiO_2* area ratios (pattern sizes of 10 μm and 40 μm) between experimental measurements and Cassie–Baxter model predictions.

Figure 12 compares the measured static contact angles and the theoretical values

predicted by the Cassie–Baxter (CB) model for SiO_2/FT-SAM and SiO_2/SiO_2* biphasic substrates under small droplet conditions (1.8 μL), across different pattern edge lengths (10 μm and 40 μm) and surface coverage ratios (0–100%). The results show that, for the SiO_2/FT-SAM system, the contact angle increases steadily with increasing FT-SAM coverage. Notably, over the coverage range of 0%–75%, all measured values are higher than the theoretical predictions for FT-SAM. This phenomenon indicates that FT-SAM possesses an extremely low surface energy (approximately 10–20 mN/m), effectively supporting localized air cushion structures. Even when the coverage ratio has not fully dominated the droplet wetting behavior, it prevents droplet penetration into the hydrophilic SiO_2 region, significantly enhancing the overall apparent contact angle. In other words, the chemical modification by FT-SAM not only provides a stable hydrophobic interface but also promotes the maintenance of the CB state.

In contrast, the SiO_2/SiO_2* system exhibits a distinctly different wetting trend. Within the 0–75% coverage range, the contact angle not only fails to increase with coverage but instead shows a decreasing trend, with overall contact angles significantly lower than those predicted by the CB model, especially at 75% coverage where the deviation is most pronounced. This result reflects that although RIE etching imparts micro/nanoscale roughness to the SiO_2* region, theoretically serving as a "gas phase support area," its inherently higher surface energy (>50 mN/m) prevents sustained air entrapment. When droplets contact the rough SiO_2* surface, they easily penetrate the structure, causing localized wetting and rapid collapse of the CB state, shifting toward the Wenzel or mixed wetting states. As the coverage of the rough area increases, gas escape intensifies and droplet penetrability increases, further reducing the overall contact angle. Due to the synergistic effect of chemically low surface energy and

microstructure, the FT-SAM system can effectively achieve a near-ideal CB state, with measured contact angles not only matching but even surpassing theoretical predictions. Conversely, the SiO_2/SiO_2* system, due to its inherently high surface energy and insufficient structural stability, struggles to maintain a non-wetting state. Despite the roughness, its wetting behavior significantly deviates from CB model predictions. This outcome emphasizes that surface design must consider both "geometric morphology" and "surface chemistry." Relying solely on rough structures is insufficient to achieve stable superhydrophobicity. This study not only reveals the limitations of the CB model for wetting behavior on non-ideal biphasic solid surfaces but also provides practical guidance for the design of functional biphasic surfaces, highlighting the critical role of synergistic control of chemical and physical properties.

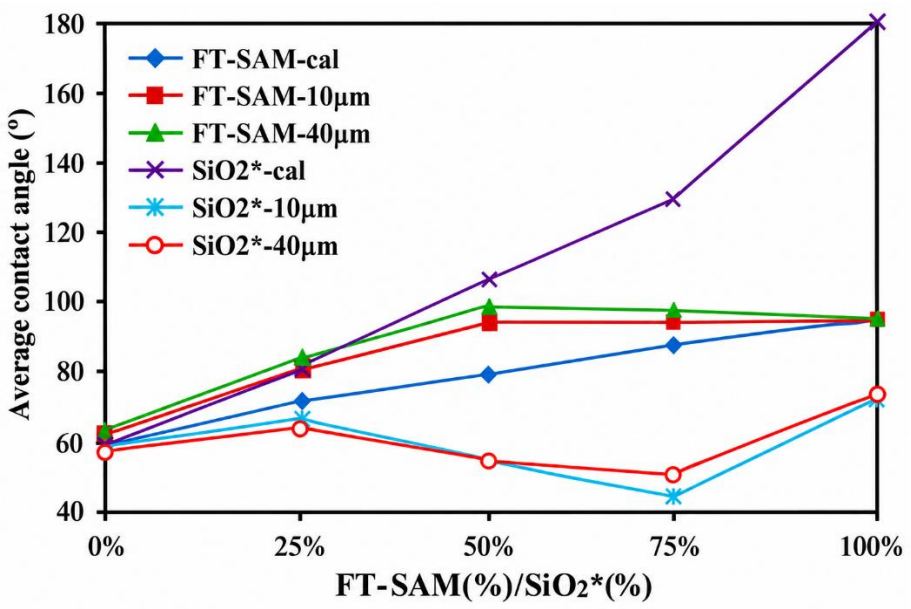


Figure 12. compares the experimentally measured average static contact angles using small water droplets (1.8 μL) on substrates with varying area fractions of the second phase (FT-SAM or SiO_2*) against the theoretical contact angle values derived from the Cassie–Baxter (CB) model.

3.3 Microstructure and Contact Angle Analysis of SiO_2/SiO_2*-FT-SAM Biphasic Substrates

SEM images of the SiO_2/SiO_2*-FT-SAM biphasic substrates show a distinct difference in surface morphology between the RIE-etched SiO_2* regions and the untreated flat SiO_2 areas. The overall pattern contours are like those previously observed for the SiO_2/SiO_2* biphasic substrates (Figure 10), exhibiting regular micron-scale roughness structures, confirming good process reproducibility. On the other hand, FT-SAM (F13-TCS) is an ultrathin organic self-assembled monolayer only a few nanometers thick, with very low electron signal contrast. Even though it is covalently bonded to the SiO_2* surface, no obvious interface difference can be observed in SEM images. Therefore, while the SAM modification alters surface chemical properties, it does not affect the material's topological structure, making it difficult to distinguish modified from unmodified regions in SEM. Static contact angle data for the SiO_2/SiO_2*-FT-SAM biphasic substrates under different pattern edge lengths (10 μm and 40 μm) and droplet volumes (1.8 μL and 6.6 μL) are summarized in Table 5 and Figure 13. The results show a significant increase in contact angle with increasing hydrophobic phase (SiO_2*-FT-SAM) coverage, consistent with multiphase wetting theory expectations. According to the Cassie–Baxter (CB) model: $\cos\theta_{CB}=f1\cos\theta1+f2\cos\theta2$, where $f1$ is the area fraction of the hydrophilic SiO_2 region, $f2=1-f1$ is the area fraction of the hydrophobic SiO_2*-FT-SAM region, and $\theta1$ and $\theta2$ are their respective intrinsic contact angles. In this study, the pure SiO_2 contact angle is approximately 58°–61°, and the SiO_2*-FT-SAM hydrophobic region is about 138°–140°. Substituting these values into the model allows calculation of theoretical contact angles at different coverage ratios, matching the

measured trends: as hydrophobic coverage increases, contact angle rises significantly, especially between 75% and 100% coverage, where droplets exhibit a stable CB state with contact angles exceeding 120°. Notably, under high hydrophobic coverage and large pattern scale conditions (40 μm, 100% coverage), the measured contact angle slightly surpasses the theoretical maximum of pure SiO_2*-FT-SAM (e.g., around 138° for small droplet volumes). This phenomenon may result from enhanced air entrapment effects among microstructures, reinforcing the air cushion support, causing the droplet to primarily contact the hydrophobic area and air interface, thereby further increasing the apparent contact angle.

Droplet volume also significantly affects wetting behavior stability. Small droplets (SD, 1.8 μL) generally exhibit higher contact angles than large droplets (LD, 6.6 μL), with this difference particularly pronounced at high hydrophobic coverage. For example, under 40 μm pattern size and 100% coverage, the SD contact angle is about 138°, whereas the LD contact angle is only about 117°. It is speculated that larger droplets experience greater bottom pressure due to gravity, which tends to disrupt the air cushion structure, causing partial droplet penetration or transition to the Wenzel state and resulting in reduced contact angles. Conversely, smaller droplets are dominated by surface tension and can maintain a stable air cushion structure. When hydrophobic coverage is insufficient (<50%, especially 25% or 0%), the contact angle decreases significantly, indicating that the hydrophobic area is inadequate to support the CB state. The droplet mainly wets the hydrophilic SiO_2 region, with overall wetting behavior approaching the Wenzel or fully wetted state.

Table 5 Comparison of the average static contact angles of SiO_2/SiO_2*- FT-SAM biphasic substrates under different droplet volumes and SiO_2* coverage ratios. Small

droplets (SD) have a volume of 1.8 μL, and large droplets (LD) have a volume of 6.6 μL.

Side length / SiO_2*-FT-SAM%	Contact angle(°)			
	10μm		40μm	
	SD	LD	SD	LD
100	135	116	138	117
75	136	115	138	118
50	128	110	132	115
25	95	90	96	92
0	61	61	58	58

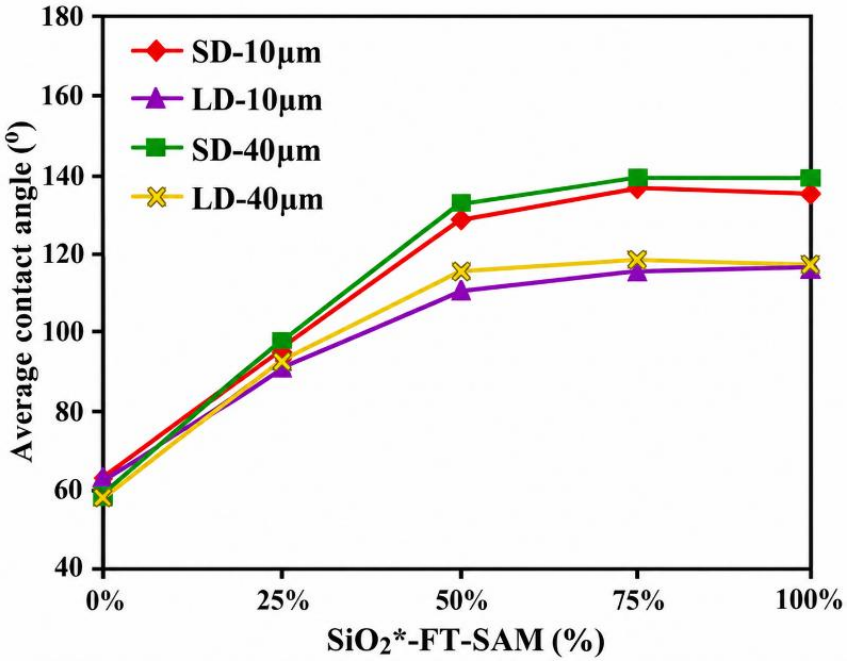


Figure 13. Average static contact angles of SiO_2/SiO_2*-FT-SAM biphasic substrates at different SiO_2*-FT-SAM area fractions.

3.5 Microstructure and Contact Angle Analysis of Hydrophobic Thin Films

In this study, large-area hydrophobic thin films exhibiting synergistic effects of

microstructure and low surface energy were successfully fabricated by controlling the relative humidity (RH) during UV curing and applying dew point pretreatment conditions. Figure 14 presents the surface morphologies and corresponding static contact angles of two sample groups cured under different conditions. Sample 1 (Figure 14(a)) was cured at RH = 60% without dew point treatment. Its surface was nearly flat, with a static contact angle of approximately 78°, characteristic of a typical Wenzel wetting state. Under this condition, the absence of condensed water led to uniform polymerization of the UV resin, without forming obvious pores or microstructures. In contrast, Sample 2 (Figure 14(b)) was cured at RH = 70% after a two-stage dew point pretreatment (16 °C and 18 °C, 1 minute each). Its surface exhibited a distinct honeycomb-like microstructure composed of numerous uniformly sized and densely packed shallow pits, significantly increasing surface roughness. This sample showed a static contact angle as 120°, consistent with the Cassie–Baxter (CB) wetting state. The droplet is suspended on a composite interface of gas and solid formed by the microstructures, substantially reducing the actual solid-liquid contact area. The key mechanisms leading to the notable differences in morphology and wettability are attributed to the synergistic effects of three factors:(1). Water vapor condensation: Under conditions below the dew point, water vapor condenses into transient microscopic droplets on the uncured UV resin surface, serving as nucleation centers for microstructure formation. (2). PDMS surface migration effect: The PDMS acrylate added to the UV resin, owing to its ultra-low surface energy, actively migrates to the surface before curing, promoting phase separation and enhancing condensation phenomena, which facilitates microstructure formation. (3). Photoresist and polymerization discontinuity: The micro water droplets formed by condensation locally

block UV irradiation, causing incomplete resin polymerization. After drying, shallow pit-like microstructures remain, effectively trapping gas and forming localized air cushions. When droplets contact such microstructured surfaces, trapped gas in the pits forms a supporting layer, allowing the droplet to suspend on a composite interface of solid protrusions and air, significantly enhancing the overall contact angle.

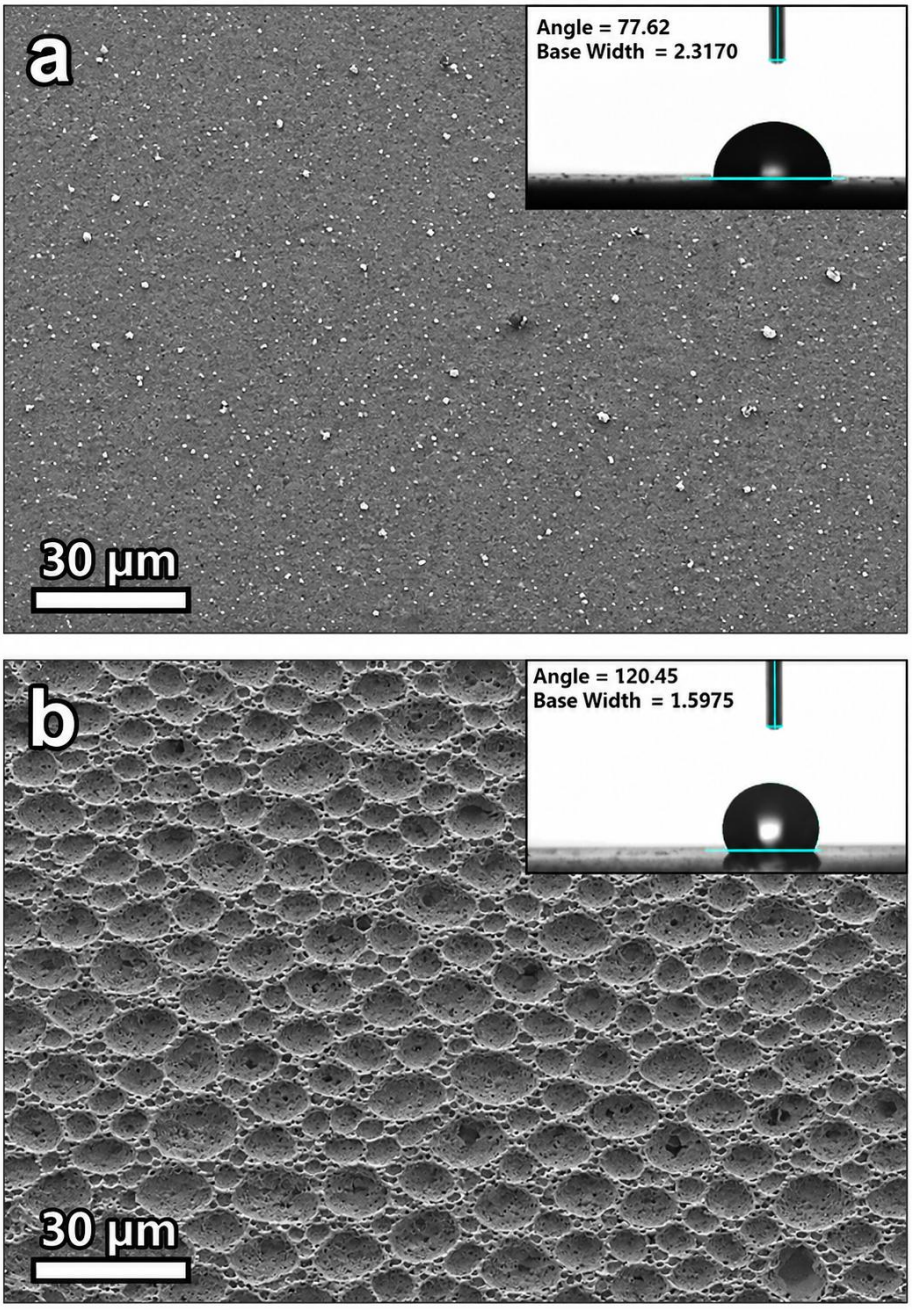


Figure 14. Contact angle measurement images of the microstructured substrate with an

air content area fraction of 25% and pattern size of 40 μm: (a) was UV cured at RH = 60% without dew point treatment; (b) was UV cured at RH = 70% after a two-stage dew point pretreatment (16 °C and 18 °C, 1 minute each)

4. Conclusion

This study developed three biphasic wettability-heterogeneous substrates based on (i) surface-energy contrast (SiO_2/FT-SAM), (ii) roughness contrast (SiO_2/SiO_2*), and (iii) their synergistic effects (SiO_2/SiO_2*-FT-SAM). The influences of pattern size, hydrophobic area fraction, and droplet volume on wetting behavior were systematically evaluated, and the applicability of established wetting models was assessed. The principal findings are summarized as follows:

1. SiO_2/FT-SAM exhibited stable and reproducible non-wetting behavior. When hydrophobic coverage exceeded 50%, the contact angle increased markedly and was consistent with the Cassie–Baxter prediction.
2. SiO_2/SiO_2* showed limited air-cushion stability despite micro-roughness; the Cassie state was only transient at 25% coverage and rapidly transitioned to the Wenzel state.
3. SiO_2/SiO_2-FT-SAM* synergistically combined roughness and low surface energy. At a pattern size of 40 μm and coverage ≥75%, the contact angle exceeded 138°, accompanied by a pronounced air-cushion effect and droplet deformation.
4. Increasing pattern size to 40 μm and reducing droplet volume to 1.8 μL improved both contact angle and wetting stability, indicating that geometric design is a key determinant of wetting regulation.

5. Dynamic airflow experiments induced a transition to a “floating” wetting state that is not captured by the conventional Cassie–Baxter model, suggesting the need for extended or alternative theoretical descriptions.
6. For large-area fabrication, hydrophobic thin films with microscale indentation structures were produced by controlling UV-curing humidity and implementing dew-point pretreatment, demonstrating reliable contact-angle tunability and process robustness.

Overall, these results demonstrate that coupling microstructural design with surface chemical modification enables effective control of wetting states and provides a foundation for engineering self-cleaning and low-adhesion surfaces.

Acknowledgments

This paper forms part of the research outcomes supported by the National Science and Technology Council (NSTC) of Taiwan. The authors gratefully acknowledge the financial support provided by the NSC.

Declarations of competing interests

The authors declare no competing financial or personal interests that could have influenced this work.

Declaration of generative AI use

ChatGPT (OpenAI, GPT-5.6 Sol) was used to assist with English-language refinement, consistency checking, and figure-label formatting during manuscript preparation. The authors reviewed and edited all outputs, verified the scientific content and references, and take full responsibility for the integrity and accuracy of the manuscript. No generative AI was used to create, alter, or replace research data or research images.

Data Availability Statement

Due to ethical and privacy considerations and to prevent unauthorized use, the data supporting the findings of this study are available from the corresponding author upon reasonable request.

5. References

Ateş A, Parizad Benam B, Mohammadilooey M, Çelik S, Serdyukov V, Surtaev A, Khalili Sadaghiani A, Koşar A (2023) Pool boiling heat transfer on superhydrophobic, superhydrophilic, and superbiphilic surfaces at atmospheric and sub-atmospheric pressures. Int J Heat Mass Transf 201:123582. https://doi.org/10.1016/j.ijheatmasstransfer.2022.123582

Bormashenko E (2015) Progress in understanding wetting transitions on rough surfaces. Adv Colloid Interface Sci 222:92-103. https://doi.org/10.1016/j.cis.2014.02.009

Brehm M, Scheiger JM, Welle A, Levkin PA (2020) Reversible surface wettability by silanization. Adv Mater Interfaces 7(12):1902134. https://doi.org/10.1002/admi.201902134

Cassie ABD, Baxter S (1944) Wettability of porous surfaces. Trans Faraday Soc 40:546-551. https://doi.org/10.1039/TF9444000546

Chen B, Seidel S, Hori H, Gupta M (2011) Self-assembly of pillars modified with vapor deposited polymer coatings. ACS Appl Mater Interfaces 3(11):4201-4205. https://doi.org/10.1021/am200836n

Cottin-Bizonne C, Barrat JL, Bocquet L, Charlaix E (2003) Low-friction flows of liquid at nanopatterned interfaces. Nat Mater 2(4):237-240. https://doi.org/10.1038/nmat857

Descamps P, Iker J, Wolf AT (1996) Effects of anodized aluminium surface parameters on the long-term adhesion of silicone structural glazing sealants. Constr Build Mater 10(7):527-538. https://doi.org/10.1016/0950-0618(96)00008-6

Drelich J (1999) Instability of the three-phase contact region and its effect on contact angle relaxation. J Adhes Sci Technol 13(12):1437-1455. https://doi.org/10.1163/156856199X00578

Drelich J, Miller JD (1993) Modification of the Cassie equation. Langmuir 9(2):619-621. https://doi.org/10.1021/la00026a043

Drelich J, Miller JD, Good RJ (1996) The effect of drop (bubble) size on advancing and receding contact angles for heterogeneous and rough solid surfaces as observed with sessile-drop and captive-bubble techniques. J Colloid Interface Sci 179(1):37-50. https://doi.org/10.1006/jcis.1996.0186

Genzer J, Efimenko K (2000) Creating long-lived superhydrophobic polymer surfaces through mechanically assembled monolayers. Science 290(5499):2130-2133. https://doi.org/10.1126/science.290.5499.2130

Haynes CL, Van Duyne RP (2001) Nanosphere lithography: a versatile nanofabrication tool for studies of size-dependent nanoparticle optics. J Phys Chem B 105(24):5599-5611. https://doi.org/10.1021/jp010657m

Hooda A, Goyat MS, Pandey JK, Kumar A, Gupta R (2020) A review on fundamentals, constraints and fabrication techniques of superhydrophobic coatings. Prog Org Coat 142:105557. https://doi.org/10.1016/j.porgcoat.2020.105557

Hoshian S, Jokinen V, Somerkivi V, Lokanathan AR, Franssila S (2015) Robust superhydrophobic silicon without a low surface-energy hydrophobic coating. ACS Appl Mater Interfaces 7(1):941-949. https://doi.org/10.1021/am507584j

Hsieh CT, Chen JM, Kuo RR, Lin TS, Wu CF (2005) Influence of surface roughness on water- and oil-repellent surfaces coated with nanoparticles. Appl Surf Sci 240(1-4):318-326. https://doi.org/10.1016/j.apsusc.2004.07.016

Jung GY, Li Z, Wu W, Chen Y, Olynick DL, Wang SY, Tong WM, Williams RS (2005) Vapor-phase self-assembled monolayer for improved mold release in nanoimprint lithography. Langmuir 21(4):1158-1161. https://doi.org/10.1021/la0476938

Kim HM, Sohn S, Ahn JS (2013) Transparent and super-hydrophobic properties of PTFE films coated on glass substrate using RF-magnetron sputtering and Cat-CVD methods. Surf Coat Technol 228(Suppl 1):S389-S392. https://doi.org/10.1016/j.surfcoat.2012.05.085

Liu J, Ye L, Wooh S, Kappl M, Steffen W, Butt HJ (2019) Optimizing hydrophobicity and photocatalytic activity of PDMS-coated titanium dioxide. ACS Appl Mater Interfaces 11(30):27422-27425. https://doi.org/10.1021/acsami.9b07490

Liu J, Fang X, Zhu C, Xing X, Cui G, Li Z (2020) Fabrication of superhydrophobic coatings for corrosion protection by electrodeposition: a comprehensive review. Colloids Surf A Physicochem Eng Asp 607:125498. https://doi.org/10.1016/j.colsurfa.2020.125498

Onoe H, Matsumoto K, Shimoyama I (2004) Three-dimensional micro-self-assembly using hydrophobic interaction controlled by self-assembled monolayers. J Microelectromech Syst 13(4):603-611. https://doi.org/10.1109/JMEMS.2004.832183

Pozzato A, Dal Zilio S, Fois G, Vendramin D, Mistura G, Belotti M, Chen Y, Natali M (2006) Superhydrophobic surfaces fabricated by nanoimprint lithography. Microelectron Eng 83(4-9):884-888. https://doi.org/10.1016/j.mee.2006.01.012

Schondelmaier D, Cramm S, Klingeler R, Morenzin J, Zilkens Ch, Eberhardt W (2002) Orientation and self-assembly of hydrophobic fluoroalkylsilanes. Langmuir 18(16):6242-6245. https://doi.org/10.1021/la0256533

Tadanaga K, Morinaga J, Matsuda A, Minami T (2000) Superhydrophobic-superhydrophilic micropatterning on flowerlike alumina coating film by the sol-gel method. Chem Mater 12(3):590-592. https://doi.org/10.1021/cm990643h

Wang H, Wang W, Wang H, Jin X, Li J, Zhu Z (2018) One-way water transport fabrics with hydrophobic rough surface formed in one-step electrospray. Mater Lett 215:110-113. https://doi.org/10.1016/j.matlet.2017.12.066

Wenzel RN (1936) Resistance of solid surfaces to wetting by water. Ind Eng Chem 28(8):988-994. https://doi.org/10.1021/ie50320a024

Young T (1805) An essay on the cohesion of fluids. Philos Trans R Soc Lond 95:65-87. https://doi.org/10.1098/rstl.1805.0005